IEICE TRANSACTIONS

on Electronics

DOI:10.1587/transele.2024MMP0001

Publicized:2024/04/09

This advance publication article will be replaced by the finalized version after proofreading.

A PUBLICATION OF THE ELECTRONICS SOCIETY

The Institute of Electronics, Information and Communication Engineers
Kikai-Shinko-Kaikan Bldg., 5-8, Shibakoen 3chome, Minato-ku, TOKYO, 105-0011 JAPAN

PAPER

Comprehensive Design Approach to Switch-Mode Resonant Power Amplifiers Exploiting Geodesic-to-Geodesic Impedance Conversion

Minoru MIZUTANI[†], ***Member and*** **Takashi OHIRA**[†], ***Fellow***

SUMMARY This paper presents a comprehensive design approach to load-independent radio frequency (RF) power amplifiers. We project the zero-voltage-switching (ZVS) and zero-voltage-derivative-switching (ZVDS) load impedances onto a Smith chart, and find that their loci exhibit geodesic arcs. We exploit a two-port reactive network to convert the geodesic locus into another geodesic. This is named geodesic-to-geodesic (G2G) impedance conversion, and the power amplifier that employs G2G conversion is called class-G2G amplifier. We comprehensively explore the possible circuit topologies, and find that there are twenty G2G networks to create class-G2G amplifiers. We also find out that the class-G2G amplifier behaves like a transformer or a gyrator converting from dc to RF. The G2G design theory is verified via a circuit simulation. We also verified the theory through an experiment employing a prototype 100 W amplifier at 6.78 MHz. We conclude that the presented design approach is quite comprehensive and useful for the future development of high-efficiency RF power amplifiers.

key words: *Class-E amplifier, load resistance deviation, Smith chart, hyperbolic geometry.*

1. Introduction

Since the early 20th century, radio-frequency (RF) power amplifiers have long been used in transmitters for broadcasting and telecommunication. The circuit topology evolution in analog power amplifiers started from class A, followed by class B, and reached class C to pursue higher and higher power-added efficiency. In the 21st century, a different application has emerged, that is, dc-to-RF power conversion for wireless power transfer (WPT) [1]. As the required WPT power level increases up to dozens of kilowatts for dynamic electric vehicle charging [2–6], the power conversion efficiency becomes much more serious than low-power WPT systems.

A technique for surpassing the classes A, B, and C in power conversion efficiency is the switch-mode amplification such as classes D, E, and F. Class D is mainly used in pulse-width modulated audio amplifiers to drive a voice-coil sound speaker. However, it might be unsuitable for WPT because it outputs rectangular-wave voltage bringing about multiple harmonics. To overcome this problem, classes E and F were invented, where the harmonics generated by the active device are reacted by lumped- or distributed-constant passive resonant elements. The reacted harmonics are exploited to enhance the dc-to-RF conversion, and thus the amplifier theoretically achieves 100% power efficiency.

The 100% efficiency of these resonant power amplifiers stems from the zero-voltage switching (ZVS) technique [7–19]. The ZVS operation indeed works, but unfortunately, only for a specific load resistance. Unless the load is exactly adjusted to the nominal resistance, the amplifier goes off from the ZVS condition and the efficiency substantially degrades [15–17]. In attempts to mitigate the effect of load resistance deviation, several reports have been made on class-E power amplifiers and inverters [20–26]. They are effective but the question still remains if there is any better solution to the load deviation problem or not. In other words, the previous works just show a particular instance of circuit topology solution. That is to say we expect a more general or comprehensive exploration on circuit topologies. Although the predecessors all seem independent approaches, we notice that they can be observed from a common theoretical viewpoint: hyperbolic geometry [27–30].

The purpose of this paper is to establish a systematic design theory for switch-mode resonant power amplifiers that can maintain ZVS operation for a wide range of load resistance. The key point is to regard the locus of load resistance as a geodesic line piece or arc projected onto a Cartesian R-X plane as well as onto the Smith chart. Lumped-constant (LC) network topologies are comprehensively explored to convert the geodesic locus into another geodesic that exactly meets the ZVS condition. This is named geodesic-to-geodesic (G2G) impedance conversion. In this paper, we call the power amplifier that employs G2G conversion a class-G2G power amplifier. Thanks to the class-G2G operation, the amplifier achieves ZVS over the full load resistance range, and even maintains its RF output voltage or current at a constant amplitude. The established design theory is verified by both circuit simulation and prototype experiment.

2. Class-E Power Amplifier Schemes

The basic scheme of the class-E amplifier is shown in Fig. 1(a). The transistor represents a high-speed semiconductor switch repeatedly turning on and off at a specified frequency e.g. 6.78 MHz. The voltage wave generated by the transistor is filtered through a series resonator $C_{\rm r}L_{\rm r}$ to deliver a sinusoidal wave to the load R_ℓ. Since we usually assume a very low on-voltage transistor, the power conversion efficiency is mainly dominated by the transistor's transient switching power loss. To minimize the switching loss, the shunt capacitor $C_{\rm s}$ and final inductor L are adjusted so that the transistor performs a ZVS operation.

Although the ZVS theoretically brings a high power

[†]The author is with Research Center for Future Vehicle City, Toyohashi University of Technology, Toyohashi, Aichi 441-8580 Japan. (email: mizutani.minoru.eu@tut.jp).

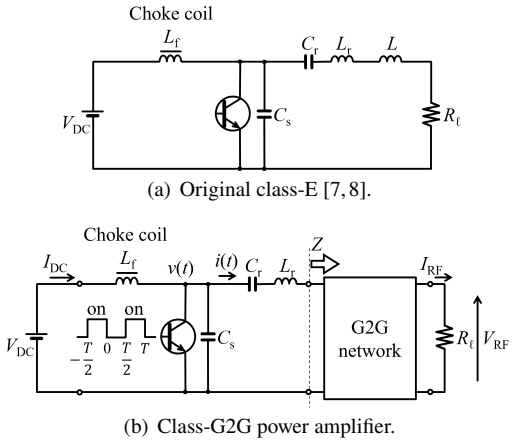

(a) Original class-E [7, 8].

(b) Class-G2G power amplifier.

Fig. 1 Class-E and class-G2G power amplifier schemes.

conversion efficiency, a practical problem still remains: the load resistance deviation. When R_ℓ deviates from its nominal resistance, the ZVS operation fails because the optimum values for C_s and L depend on R_ℓ. To address this issue, a previous research replaced the input choke coil with a finite inductor [20–26]. This technique substantially improves the load tolerance. We then have a new question as whether this scheme is the only solution to solve the load deviation problem or not. To widely seek possible solutions, we propose a generalized scheme with a black box named as G2G network as shown in Fig. 1(b). We will consider how this box should behave to meet the ZVS condition in the following sections.

3. ZVS Geodesic

Looking at Fig. 1(b), thanks to the bandpass filtering effect of series resonator C_rL_r, the current flowing into the G2G network is supposed to have a purely sinusoidal waveform, which can be expressed as

$$i(t) = I\sin(\omega t + \theta), \tag{1}$$

where I denotes the current magnitude, T the switching time period, $\omega = 2\pi/T$, and θ the phase delay. Just after the switch turns off at $t = 0$, the voltage is accumulated across the shunt capacitor C_s as

$$v(t) = \frac{1}{\omega C_s}\{I_{DC}\omega t + I(\cos(\omega t + \theta) - \cos\theta\} \tag{2}$$

until the switch turns on at $t = T/2$. This voltage waveform repeats with time period T in synchrony to the switching gate signal. Based on equations (1) and (2), a harmonic balance analysis yields

$$\pi^2 I_{DC} - 2(2\sin\theta + \pi\cos\theta)I = 4\pi\omega C_s V_{DC}, \tag{3}$$

$$(\pi\cos\theta - 2\sin\theta)I_{DC} - (2\cos^2\theta + \pi\hat{R})I = 0, \tag{4}$$

$$2(2\cos\theta + 2\pi\sin\theta)I_{DC} - (\pi + 2\sin 2\theta + 2\pi\hat{X})I = 0, \tag{5}$$

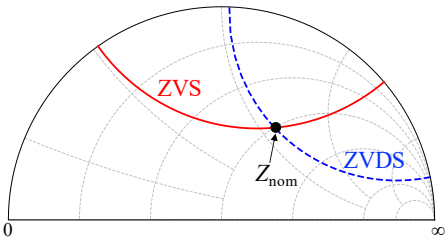

Fig. 2 ZVS and ZVDS geodesics projected onto an upper-half Smith chart.

where the hat symbol is used for the impedance normalization $\hat{R} = \omega C_s R$ and $\hat{X} = \omega C_s X$ by the shunt capacitor susceptance ωC_s. See References [16] for a rigorous derivation of (3), (4), and (5). These equations signify that the current magnitude I is linearly related to the DC supply voltage V_{DC} and current I_{DC}. To meet the ZVS condition, $v(t)$ should come down to zero at $t = T/2$. Therefore, imposing $v(T/2) = 0$ on equation (2), we obtain

$$\pi I_{DC} = 2I\cos\theta. \tag{6}$$

Now looking at the three equations (4), (5), and (6), there are three unknowns: I_{DC}, I, and θ. For the three equations to have a nontrivial solution set for the three unknowns, the G2G network must exhibit its input impedance $Z = R + jX$ that satisfies the relation

$$\hat{R}^2 + \left(\hat{X} + \frac{2}{\pi^2} - \frac{1}{2}\right)^2 = \left(\frac{2}{\pi^2}\right)^2. \tag{7}$$

As we assume a passive load, i.e., $R > 0$, equation (7) draws a semicircle on the Cartesian $R - X$ plane [16], or an arc on the Smith chart as shown in Fig. 2. This semicircle or arc is called the ZVS geodesic from hyperbolic geometry. The broken arc in Fig. 2 stems from the so-called zero voltage derivative switching (ZVDS) condition [15–17], which is formulated as

$$\hat{R}^2 + (\hat{X} - 1)^2 = \frac{4}{\pi^2} + \frac{1}{4}. \tag{8}$$

The so-called class-E amplifiers usually operate at the intersection of the two arcs, which is solved as

$$Z_{nom} = \frac{1}{\omega C_s(\pi^2 + 4)}\left(\frac{8}{\pi} + j\frac{\pi^2 - 4}{2}\right). \tag{9}$$

However, ZVDS is not always necessary to theoretically achieve the 100% efficiency, but is just an option to make good use of the freedom of load impedance. Therefore, we focus on the ZVS geodesic solely as the rule for acceptable load impedance deviation.

4. G2G Impedance Conversion

Since the box in Fig. 1(b) is supposed to be lossless, it can be modeled as a reactive network having its impedance matrix of four purely imaginary components as shown in Fig. 3.

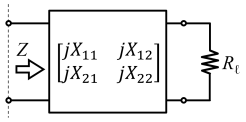

Fig. 3 General black-box model of two-port reactive network.

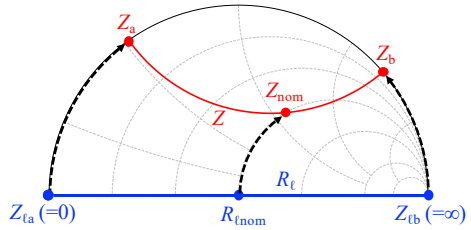

(a) CV output.

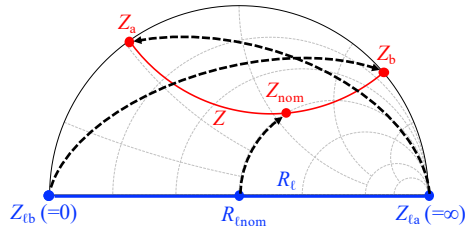

(b) CC output.

Fig. 4 Impedance comversion from resistive load geodesic to ZVS geodesic.

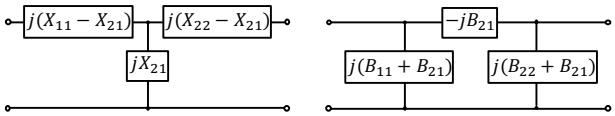

(a) T-shape. (b) π-shape.

Fig. 5 Two topologies of reactive network for G2G impedance conversion.

Thanks to reciprocity, the two off-diagonal components are equal, i.e., $X_{21} = X_{12}$. This is to say, the degree of freedom remains to be three: X_{11}, X_{21}, and X_{22}. The basic two-port circuit theory tells us that the box converts the impedance from a resistive load R_ℓ into input impedance

$$Z = jX_{11} + \frac{X_{21}^2}{jX_{22} + R_\ell}. \tag{10}$$

As equation (10) contains three parameters, we can adjust them so that Z meets the ZVS geodesic. This can be done by specifying any set of three different points to be regarded as representatives of the entire horizon. A typical set would be (0 Ω, 50 Ω, ∞ Ω), which is also known as the open-short-match calibration kit for vector network analyzers. The three points are expected to be converted into the other three points lying on the ZVS geodesic arc as shown in Fig. 4(a) or (b).

5. LC Network Variety

5.1 CV Output Network

Looking at Fig. 4(a), the horizon ends at

$$Z_{\ell a} = 0, \quad Z_{\ell b} = \infty. \tag{11}$$

These two ends are the most mathematically convenient among representatives. According to (7), these two points are respectively converted into the ends of the arc as

$$Z_a = j\frac{1}{2\omega C_s}, \quad Z_b = j\frac{\pi^2 - 8}{2\pi^2 \omega C_s}. \tag{12}$$

In addition to the two points, we can specify the nominal point $R_{\ell nom}$ anywhere on the horizon, say 50 Ω, which is converted into Z_{nom} on the arc. To the three points, equation (10) is applied as

$$Z_a = jX_{11} + \frac{X_{21}^2}{jX_{22} + Z_{\ell a}}, \tag{13}$$

$$Z_b = jX_{11} + \frac{X_{21}^2}{jX_{22} + Z_{\ell b}}, \tag{14}$$

$$Z_{nom} = jX_{11} + \frac{X_{21}^2}{jX_{22} + R_{\ell nom}}. \tag{15}$$

To meet (11)-(15), the three reactances should come to

$$X_{11} = \frac{1}{2\omega C_s}, \tag{16}$$

$$X_{21} = \pm\sqrt{\frac{2R_{\ell nom}}{\pi\omega C_s}}, \tag{17}$$

$$X_{22} = \frac{\pi}{2} R_{\ell nom}. \tag{18}$$

As we know the T-shaped topology in Fig. 5(a) to exhibit X_{11}, X_{21}, and X_{22}, feasible LC network instances are listed in Table 1. Thanks to the duality theorem between Z- and Y-parameters, the above three reactances are equivalent to the three susceptances

$$B_{11} = -\frac{2\pi^2\omega C_s}{\pi^2 - 8}, \tag{19}$$

$$B_{21} = \pm\frac{4}{\pi^2 - 8}\sqrt{\frac{2\pi\omega C_s}{R_{\ell nom}}}, \tag{20}$$

$$B_{22} = -\frac{2\pi}{\pi^2 - 8}\frac{1}{R_{\ell nom}}, \tag{21}$$

which can be exhibited by the π-shaped topology in Fig. 5(b), and its feasible LC network instances are also listed in Table 1. The ten solutions shown in this table all carry out the ZVS operation over the full range of load resistance.

Another concern is how the RF output voltage behaves when the load resistance changes. Substituting (16)-(18) into (10), the input impedance results in

$$Z = jX_{11} + \frac{X_{12}X_{21}}{jX_{22} + R_\ell} = \frac{16R_\ell R_{\ell\mathrm{nom}} + j\pi\{4R_\ell^2 + (\pi^2-8)R_{\ell\mathrm{nom}}^2\}}{2\pi\omega C_\mathrm{s}(4R_\ell^2 + \pi^2 R_{\ell\mathrm{nom}}^2)}. \quad (22)$$

Then substituting (22) into (3)-(5), the output current becomes

$$I = \frac{\pi\omega C_\mathrm{s}\sqrt{4R_\ell^2 + \pi^2 R_{\ell\mathrm{nom}}^2}}{2R_\ell} V_\mathrm{DC}. \quad (23)$$

Finally recalling the definition of Z-parameters, the output voltage is obtained as

$$V_\mathrm{RF} = \left|\frac{jX_{21}R_\ell}{jX_{22} + R_\ell}\right| I = \sqrt{2\pi\omega C_\mathrm{s} R_{\ell\mathrm{nom}}}\, V_\mathrm{DC}. \quad (24)$$

We find that the final right-hand side does not include R_ℓ. This result signifies that the amplifier's RF output voltage stays constant even when the load resistance changes.

5.2 CC Output Network

Looking at Fig. 4(b), the horizon is ended at

$$Z_{\ell\mathrm{a}} = \infty, \quad Z_{\ell\mathrm{b}} = 0. \quad (25)$$

These two ends are the most mathematically convenient among representatives. Similar to the CV output, these two points are respectively converted into the ends of the arc as (12). In addition to the two points, we can specify the nominal point $R_{\ell\mathrm{nom}}$ anywhere on the horizon, say 50 Ω, which is converted into Z_nom on the arc. Putting the horizontal three points and those on the ZVS geodesic arc into (13)−(15), we derive the Z-parameters as

$$X_{11} = \frac{\pi^2 - 8}{2\pi^2\omega C_\mathrm{s}}, \quad (26)$$

$$X_{21} = \pm\frac{2}{\pi}\sqrt{\frac{2R_{\ell\mathrm{nom}}}{\pi\omega C_\mathrm{s}}}, \quad (27)$$

$$X_{22} = -\frac{2}{\pi}R_{\ell\mathrm{nom}}. \quad (28)$$

As we know the T-shaped topology in Fig. 5(a) to exhibit X_{11}, X_{21}, and X_{22}, feasible LC network instances are listed in Table 2. Thanks to the duality theorem between Z- and Y-parameters, the above three reactances are equivalent to the three susceptances

$$B_{11} = -2\pi\omega C_\mathrm{s}, \quad (29)$$

$$B_{21} = \mp 2\sqrt{\frac{2\omega C_\mathrm{s}}{\pi R_{\ell\mathrm{nom}}}}, \quad (30)$$

$$B_{22} = \frac{\pi^2 - 8}{2\pi R_{\ell\mathrm{nom}}}, \quad (31)$$

which can be exhibited by the π-shaped topology in Fig. 5(b), and its feasible LC network instances are also listed in Table 2. The ten solutions shown in this table all carry out the ZVS operation over the full range of load resistance.

Another concern is how the RF output current behaves when the load resistance changes. Substituting (26)-(28) into (10), the input impedance results in

$$Z = \frac{16R_\ell R_{\ell\mathrm{nom}} + j\pi\{4R_{\ell\mathrm{nom}}^2 + (\pi^2-8)R_\ell^2\}}{2\pi\omega C_\mathrm{s}(4R_{\ell\mathrm{nom}}^2 + \pi^2 R_\ell^2)}. \quad (32)$$

Then substituting (32) into (3)-(5), the output current becomes

$$I = \frac{\pi\omega C_\mathrm{s}\sqrt{4R_{\ell\mathrm{nom}}^2 + \pi^2 R_\ell^2}}{2R_{\ell\mathrm{nom}}} V_\mathrm{DC}. \quad (33)$$

Finally, recalling the definition of Z-parameters, the output current is obtained as

$$I_\mathrm{RF} = \left|\frac{jX_{21}}{jX_{22} + R_\ell}\right| I = \sqrt{\frac{2\pi\omega C_\mathrm{s}}{R_{\ell\mathrm{nom}}}}\, V_\mathrm{DC}. \quad (34)$$

We find that the final right-hand side does not include R_ℓ. This result signifies that the amplifier's RF output current stays constant even when the load resistance changes.

Tables 1 and 2 comprehensively cover circuit topologies in addition to all the previous works [20–26]. The class-G2G amplifier is a general concept intended to unify the variety of possible circuit topologies.

5.3 DC-to-RF Matrix

Even though switch-mode amplifiers have strong nonlinearity due to the switching device, a different theoretical approach was found by linear algebra to address the behavior of class-E power amplifiers [15]. We hereby take a similar matrix approach to class-G2G amplifiers. Thanks to the ZVS operation, the theoretical efficiency of dc-to-RF conversion is 100%, which is formulated as

$$V_\mathrm{DC} I_\mathrm{DC} = \frac{1}{2} V_\mathrm{RF} I_\mathrm{RF}. \quad (35)$$

The factor 1/2 on the right-hand side comes from the definition of RF voltage and current in their peak not in RMS. For the CV output amplifiers, (24) can be rewritten as

$$V_\mathrm{DC} = \sqrt{\frac{R_\mathrm{DCnom}}{2R_{\ell\mathrm{nom}}}}\, V_\mathrm{RF}, \quad (36)$$

where $R_\mathrm{DCnom} = 1/(\pi\omega C_\mathrm{s})$ signifies the dc input resistance under simultaneous ZVS and ZVDS conditions [15]. Substituting (36) into (35), we get the current relation

$$I_\mathrm{DC} = \sqrt{\frac{R_{\ell\mathrm{nom}}}{2R_\mathrm{DCnom}}}\, I_\mathrm{RF}. \quad (37)$$

The relations (36) and (37) merge into a single matrix form

$$\begin{pmatrix} V_\mathrm{DC} \\ I_\mathrm{DC} \end{pmatrix} = \frac{1}{\sqrt{2}} \begin{pmatrix} \sqrt{\frac{R_\mathrm{DCnom}}{R_{\ell\mathrm{nom}}}} & 0 \\ 0 & \sqrt{\frac{R_{\ell\mathrm{nom}}}{R_\mathrm{DCnom}}} \end{pmatrix} \begin{pmatrix} V_\mathrm{RF} \\ I_\mathrm{RF} \end{pmatrix}. \quad (38)$$

Table 1 Ten alternative solutions of reactive network for CV output.

<table>
<tr><td colspan="5">$X_{21} > 0, B_{21} > 0$</td><td>$X_{21} < 0, B_{21} < 0$</td></tr>
<tr><td>$0 < R_{\ell\mathrm{nom}} < \frac{8}{\pi^3\omega C_\mathrm{s}}$</td><td>$R_{\ell\mathrm{nom}} = \frac{8}{\pi^3\omega C_\mathrm{s}}$</td><td>$\frac{8}{\pi^3\omega C_\mathrm{s}} < R_{\ell\mathrm{nom}} < \frac{\pi}{8\omega C_\mathrm{s}}$</td><td>$R_{\ell\mathrm{nom}} = \frac{\pi}{8\omega C_\mathrm{s}}$</td><td>$\frac{\pi}{8\omega C_\mathrm{s}} < R_{\ell\mathrm{nom}} < \infty$</td><td>$0 < R_{\ell\mathrm{nom}} < \infty$</td></tr>
<tr><td>$0 < \frac{V_\mathrm{RF}}{V_\mathrm{DC}} < \frac{4}{\pi}$</td><td>$\frac{V_\mathrm{RF}}{V_\mathrm{DC}} = \frac{4}{\pi}$</td><td>$\frac{4}{\pi} < \frac{V_\mathrm{RF}}{V_\mathrm{DC}} < \frac{\pi}{2}$</td><td>$\frac{V_\mathrm{RF}}{V_\mathrm{DC}} = \frac{\pi}{2}$</td><td>$\frac{\pi}{2} < \frac{V_\mathrm{RF}}{V_\mathrm{DC}} < \infty$</td><td>$0 < \frac{V_\mathrm{RF}}{V_\mathrm{DC}} < \infty$</td></tr>
<tr><td> 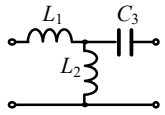
LLC</td><td rowspan="2"> 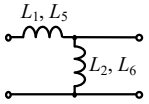
LL-1</td><td> 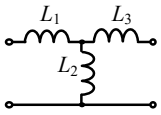
LLL</td><td rowspan="2"> 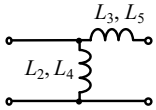
LL-2</td><td> 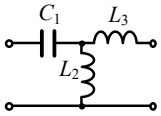
CLL</td><td> 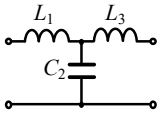
LCL</td></tr>
<tr><td> 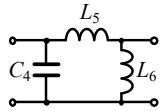
CLL</td><td> 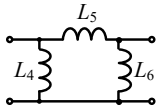
LLL</td><td> 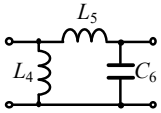
LLC</td><td> 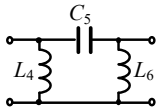
LCL</td></tr>
<tr><td colspan="6">$\omega L_1 = X_{11} - X_{21}, \quad \frac{1}{\omega C_1} = X_{21} - X_{11}, \quad \omega L_2 = X_{21}, \quad \frac{1}{\omega C_2} = -X_{21}, \quad \omega L_3 = X_{22} - X_{21}, \quad \frac{1}{\omega C_3} = X_{21} - X_{22}$</td></tr>
<tr><td colspan="6">$\omega C_4 = B_{11} + B_{21}, \quad \frac{1}{\omega L_4} = -(B_{11} + B_{21}), \quad \omega C_5 = -B_{21}, \quad \frac{1}{\omega L_5} = B_{21}, \quad \omega C_6 = B_{22} + B_{21}, \quad \frac{1}{\omega L_6} = -(B_{22} + B_{21})$</td></tr>
</table>

Table 2 Ten alternative solutions of reactive network for CC output.

<table>
<tr><td colspan="3">$X_{21} < 0, B_{21} > 0$</td><td colspan="3">$X_{21} > 0, B_{21} < 0$</td></tr>
<tr><td>$0 < R_{\ell\mathrm{nom}} < \frac{2}{\pi\omega C_\mathrm{s}}$</td><td>$R_{\ell\mathrm{nom}} = \frac{2}{\pi\omega C_\mathrm{s}}$</td><td>$\frac{2}{\pi\omega C_\mathrm{s}} < R_{\ell\mathrm{nom}} < \infty$</td><td>$0 < R_{\ell\mathrm{nom}} < \frac{(\pi^2-8)^2}{32\pi\omega C_\mathrm{s}}$</td><td>$R_{\ell\mathrm{nom}} = \frac{(\pi^2-8)^2}{32\pi\omega C_\mathrm{s}}$</td><td>$\frac{(\pi^2-8)^2}{32\pi\omega C_\mathrm{s}} < R_{\ell\mathrm{nom}} < \infty$</td></tr>
<tr><td>$\infty > \frac{I_\mathrm{RF}}{V_\mathrm{DC}} > \pi\omega C_\mathrm{s}$</td><td>$\frac{I_\mathrm{RF}}{V_\mathrm{DC}} = \pi\omega C_\mathrm{s}$</td><td>$\pi\omega C_\mathrm{s} > \frac{I_\mathrm{RF}}{V_\mathrm{DC}} > 0$</td><td>$\infty > \frac{I_\mathrm{RF}}{V_\mathrm{DC}} > \frac{8\pi\omega C_\mathrm{s}}{\pi^2-8}$</td><td>$\frac{I_\mathrm{RF}}{V_\mathrm{DC}} = \frac{8\pi\omega C_\mathrm{s}}{\pi^2-8}$</td><td>$\frac{8\pi\omega C_\mathrm{s}}{\pi^2-8} > \frac{I_\mathrm{RF}}{V_\mathrm{DC}} > 0$</td></tr>
<tr><td> 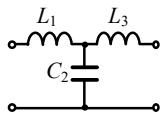
LCL</td><td rowspan="2"> 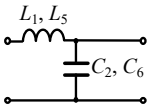
LC-1</td><td> 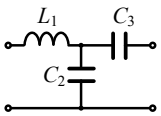
LCC</td><td> 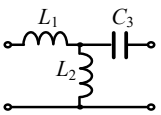
LLC</td><td rowspan="2"> 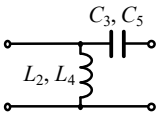
LC-2</td><td> 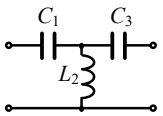
CLC</td></tr>
<tr><td> 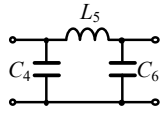
CLC</td><td> 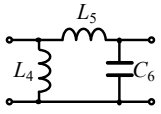
LLC</td><td> 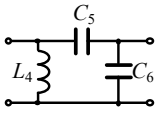
LCC</td><td> 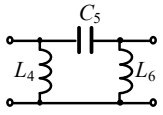
LCL</td></tr>
<tr><td colspan="6">$\omega L_1 = X_{11} - X_{21}, \quad \frac{1}{\omega C_1} = X_{21} - X_{11}, \quad \omega L_2 = X_{21}, \quad \frac{1}{\omega C_2} = -X_{21}, \quad \omega L_3 = X_{22} - X_{21}, \quad \frac{1}{\omega C_3} = X_{21} - X_{22}$</td></tr>
<tr><td colspan="6">$\omega C_4 = B_{11} + B_{21}, \quad \frac{1}{\omega L_4} = -(B_{11} + B_{21}), \quad \omega C_5 = -B_{21}, \quad \frac{1}{\omega L_5} = B_{21}, \quad \omega C_6 = B_{22} + B_{21}, \quad \frac{1}{\omega L_6} = -(B_{22} + B_{21})$</td></tr>
</table>

Table 3 Circuit parameters for simulation and experiment with GaN FET

Parameter	Symbol	Unit	Value			
			CV output (Fig. 1(b) and LCL topology from Table 1)		CC output (Fig. 1(b) and LCL topology from Table 2)	
			Sim.	Exp.	Sim.	Exp.
Transistor	-	-	PGA26E07BA (Panasonic)			
Switching frequency	f_{sw}	MHz	6.78			
DC supply voltage	V_{DC}	V	48			
Duty cycle	D	%	50			
RF choke inductor	L_f	μH	10			
Shunt capacitor	C_s	pF	226	220	226	220
Resonant capacitor	C_r	pF	200			
Resonant inductor	L_r	μH	2.76	2.9	2.76	2.9
G2G Inductor	L_1	μH	1.43	1.3	0.53	0.41
G2G Capacitor	C_2	pF	948	1210	1490	1850
G2G Inductor	L_3	μH	1.07	0.85	0.17	0.11

Looking at the 2×2 matrix, we notice that the two diagonal components are multiplicative inverses to each other. We also notice that the off-diagonal components are both zero. Therefore, we can conclude that this network equivalently acts as a transformer. It should be emphasized that this is not a usual AC-to-AC but dc-to-RF transformer.

For the CC-output amplifiers, we can rewrite (34) to

$$V_{DC} = \sqrt{\frac{R_{DCnom} R_{\ell nom}}{2}} I_{RF}. \tag{39}$$

Substituting (39) into (35), we get the current and voltage relation

$$I_{DC} = \frac{1}{\sqrt{2 R_{DCnom} R_{\ell nom}}} V_{RF}. \tag{40}$$

The relations (39) and (40) merge into a single matrix form

$$\begin{pmatrix} V_{DC} \\ I_{DC} \end{pmatrix} = \frac{1}{\sqrt{2}} \begin{pmatrix} 0 & \sqrt{R_{DCnom} R_{\ell nom}} \\ \dfrac{1}{\sqrt{R_{DCnom} R_{\ell nom}}} & 0 \end{pmatrix} \begin{pmatrix} V_{RF} \\ I_{RF} \end{pmatrix}. \tag{41}$$

Looking at the 2×2 matrix, we notice that the two off-diagonal components are multiplicative inverses to each other. We also notice that the two diagonal components are both zero. Therefore, we can conclude that this network equivalently acts as a gyrator. It should be emphasized that this is not the usual AC-to-AC but dc-to-RF gyrator.

6. Proof by Simulation and Experiment

6.1 Simulation

To prove the G2G theory, we carry out a circuit simulation using LTSPICE. The circuit for simulation is shown in Fig. 1(b), in which the G2G network employs the T-shape LCL topology from Table 1 or 2. The simulation parameters are shown in Table 3. The circuit design procedure step by step is:

Step 1 Give the specification of the amplifier: DC voltage V_{DC}, RF output power P_o, nominal RF load resistance $R_{\ell nom}$, and switching frequency f_{sw}.

Step 2 According to $P_o = \pi \omega C_s$ [15], find shunt capacitor value C_s. Note that $\omega = 2\pi f_{sw}$.

Step 3 Specify L_r and C_r to meet $\omega^2 L_r C_r = 1$.

Step 4a Substituting ωC_s and $R_{\ell nom}$ into (16)-(18), find the Z parameters of the G2G network for CV output.

Step 4b Substituting ωC_s and $R_{\ell nom}$ into (26)-(28), find the Z parameters of the G2G network for CC output.

Step 5a Putting the Z parameters of the G2G network into $\omega L_1 = X_{11} - X_{21}$, $\dfrac{1}{\omega C_2} = -X_{21}$, and $\omega L_3 = X_{22} - X_{21}$ in Table 1, find L_1, C_2, and L_3 for CV output.

Step 5b Putting the Z parameters of the G2G network into $\omega L_1 = X_{11} - X_{21}$, $\dfrac{1}{\omega C_2} = -X_{21}$, and $\omega L_3 = X_{22} - X_{21}$ in Table 2, find L_1, C_2, and L_3 for CC output.

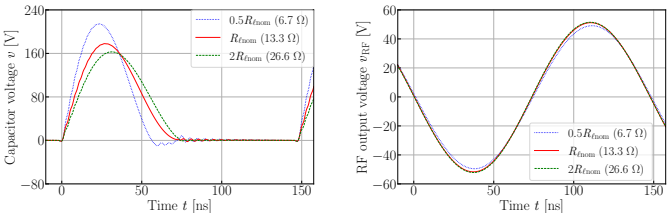

(a) Capacitor voltage. (b) RF output voltage.

Fig. 6 Simulation results of CV output.

The simulation results for CV output are shown in Figs. 6(a) and 6(b). From these figures, we can conclude that the proof is successful. This is because the simulation result (Figure 6(a)) finds a ZVS operation over the specified load resistance range from 6.7 Ω to 26.6 Ω. Another evidence of this success is that the result (Figure 6(b)) shows that the amplifier keeps a constant output voltage amplitude against the same load variation.

The simulation results for CC output are shown in Figs. 7(a) and 7(b). We can have the same conclusion as the CV output case that the G2G theory is successfully proved also for CC output.

6.2 Experiment

In addition to the above simulation, we prove the G2G theory also by experiment. Figure 8 shows the experimental setup. As the key component of this experiment, we develop a 6.78

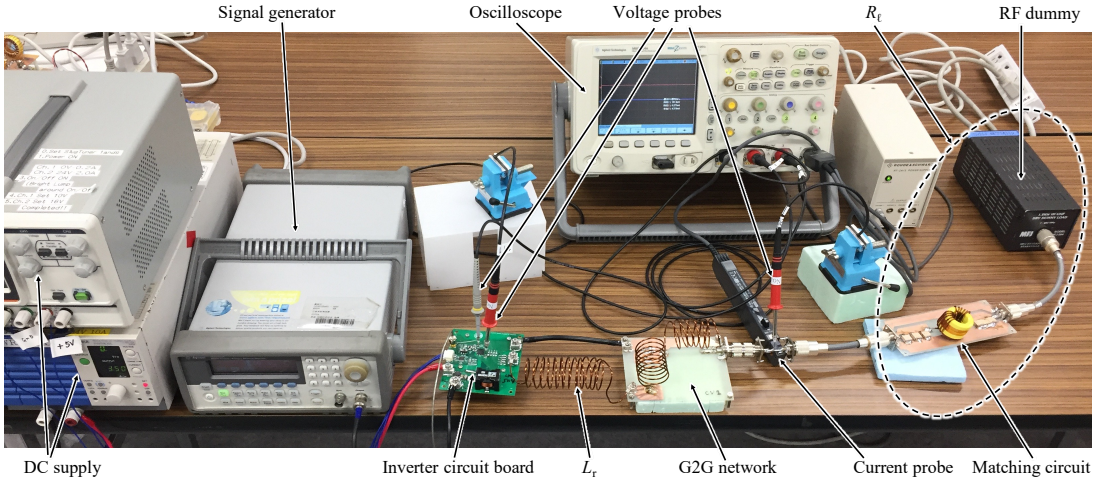

Fig. 8 Experimental setup.

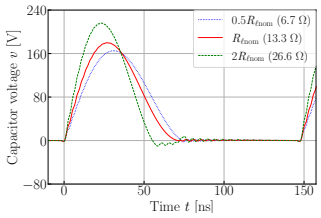

(a) Capacitor voltage.

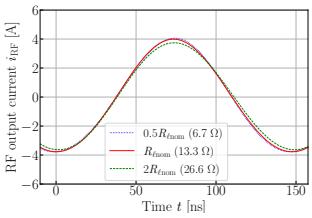

(b) RF output current.

Fig. 7 Simulation results of CC output.

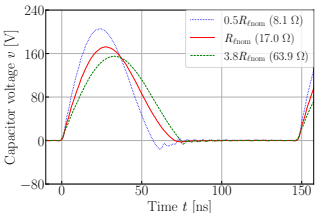

(a) Capacitor voltage.

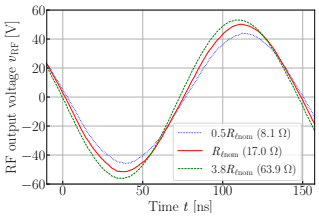

(b) RF output voltage.

Fig. 10 Experimental results of CV output.

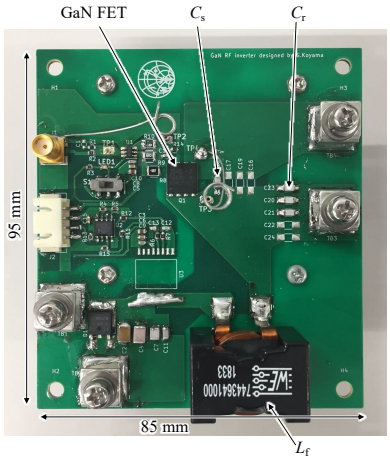

Fig. 9 Closer look at prototype RF amplifier circuit board (6.78 MHz, 100 W).

MHz 100 W class RF amplifier circuit board as shown in Fig. 9. We employ a GaN FET PGA26E07BA (Panasonic) as the transistor. We prototype two G2G networks for CV and CC output. We use a variable resistive load consisting of an adjustable matching circuit and a 50 Ω fixed RF dummy. The experimental parameters are shown in Table 3. We observe the shunt capacitor voltage, RF output voltage, and current waveforms using RF probes in time domain.

The experimental results for CV output are shown in Figs. 10(a) and 10(b). Figure 10(a) shows the shunt capacitor voltage waveforms. This result signifies that the amplifier suceeds in keeping the ZVS operation over the wide load resistance range from 8.1 to 63.9 Ω. Figure 10(b) shows the RF output voltage waveforms. The RF output voltage is kept at 48.1 V within ±4.93 V deviation over the same load resistance range.

The experimental results for CC output are shown in Figs. 11(a) and 11(b). Figure 11(a) shows the shunt capacitor voltage waveforms. This result signifies that the amplifier suceeds in keeping the ZVS operation over the wide load resistance range from 5.0 to 25.0 Ω. Figure 11(b) shows the RF output current waveforms. The RF output voltage is kept at 3.86 A within ±0.23 A deviation over the wide load resistance range from 5.0 to 25.0 Ω.

We conclude that both simulation and experiment overall prove the G2G theory.

7. Conclusion

We have exploited a two-port reactive network to transform a complex impedance from one geodesic to another. We es-

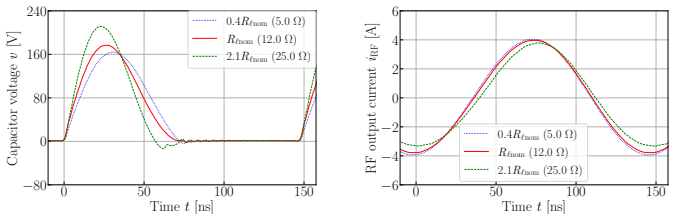

(a) Capacitor voltage. (b) RF output current.

Fig. 11 Experimental results of CC output.

tablished a design theory of G2G networks employing two or three LC elements. The G2G network enables switch-mode power amplifiers to achieve load-independent ZVS operation. The class-G2G amplifier holds its output voltage or current at a constant amplitude. We listed twenty comprehensive G2G networks to create class-G2G amplifiers. In addition, we found out that the class-G2G amplifier behaves like a transformer or a gyrator converting from dc to RF. The G2G design theory is verified via the circuit simulation on CV and CC output. We also verified the theory through experiment employing the prototype 100 W amplifier at 6.78 MHz. The presented theory is quite intuitively instructive because it is demonstrated by graphics. This work will effectively contribute to the development of load-independent high-power RF systems.

References

[1] N. Shinohara, "Power without wires," *IEEE Microw. Mag.*, vol. 12, no. 7, pp. S64-S73, Dec. 2011.

[2] N. Sakai, D. Itokazu, Y. Suzuki, S. Sakihara, and T. Ohira, "One-kilowatt capacitive power transfer via wheels of a compact electric vehicle," *IEEE Wireless Power Transfer Conf.*, Aveiro, Portugal, May 2016.

[3] N. Sakai, D. Itokazu, Y. Suzuki, S. Sakihara, and T. Ohira, "Single-seater vehicle prototype experiment powered by high frequency electric field on an asphalt-paved roadway," Electric Drives Production Conference, pp. 101-104, Nuremberg, Germany, Nov. 2016.

[4] T. Ohira, " A battery-less electric roadway vehicle runs for the first time in the world (invited)," IEEE International Conference Microwave Intelligent Mobility, pp. 75-78, Nagoya, March 2017.

[5] C. C. Mi, G. Buja, S. Y. Choi, and C. T. Rim, " Modern advances in wire-less power transfer systems for roadway powered electric vehicles," *IEEE Trans. Ind. Electron.*, vol.63, no.10, pp.6533-6545, Oct. 2016.

[6] Y. Yamada and T. Imura, " An efficiency optimization method of static wireless power transfer coreless coils for electric vehicles in the 85 kHz band using numerical analysis", *IEEJ Trans. Elec. Electron. Eng.*, vol. 17, Issue 10, pp. 1506-1516, Oct. 2022.

[7] G. D. Ewing, " High-efficiency radio-frequency power amplifiers, " Ph.D. Thesis, Oregon State University, June 1964.

[8] N. O. Sokal and A. D. Sokal, "Class E - a new class of high-efficiency tuned single-ended switching power amplifiers," *IEEE J. Solid-State Circuits*, vol. SC-10, pp. 168-176, June 1975.

[9] F. H. Raab, "Idealized operation of the class E tuned power amplifier, " *IEEE Trans. Circuits Syst. I*, vol. 24, pp. 725-735, Dec. 1977.

[10] M. K. Kazimierczuk and D. Czarkowski, *Resonant Power Converters*, pp. 334-368, Wiley, New Jersey 2011.

[11] T. Suetsugu and M. K. Kazimierczuk, "Design procedure of class-E amplifier for off-nominal operation at 50% duty ratio," *IEEE Trans. Circuits Syst. I, Reg. Papers*, vol. 53, no. 7, pp. 1468-1476, July 2006.

[12] T. Suetsugu and M. K. Kazimierczuk, " Off-nominal operation of class-E amplifier at any duty ratio, " *IEEE Trans. Circuits Syst. I, Reg. Papers*, vol. 54, no. 6, pp. 1389-1397, June 2007.

[13] Z. Popovic and J. A. Garcia, "Microwave class-E power amplifiers: a brief review of essential concepts in high-frequency class-E PAs and related circuits, " *IEEE Microw. Mag.*, vol. 19, pp. 54-66, July-Aug. 2018.

[14] A. Mediano and F. J. Ortega-Gonzalez, " Class-E amplifiers and applications at MF, HF, and VHF: examples and applications," *IEEE Microw. Mag.*, vol. 19, pp. 42-53, July-Aug. 2018.

[15] T. Ohira, " Linear algebra elucidates class-E amplifiers, " *IEEE Microw. Mag.*, vol. 23, no. 1, pp. 83-105, Jan. 2022.

[16] T. Ohira, "Load impedance perturbation formulas for class-E power amplifiers, " *IEICE Communications Express*, vol. 9, no. 10, pp. 482-488, Oct. 2020.

[17] M. Mizutani and T. Ohira, "Experimental study on the class-E power amplifier's output impedance," *IEICE Trans.*, vol. J105-C, no. 1, pp. 37-45, Jan. 2022.

[18] A. Grebennikov and F. H. Raab, "A history of switching-mode class-E techniques: the development of switching-mode class-E techniques for high-efficiency power amplification," *IEEE Microw. Mag.*, vol. 19, no. 5, pp. 26-41, July-Aug. 2018.

[19] J. Choi, D. Tsukiyama, Y. Tsuruda, and J. M. R. Davila, " High-frequency, high-power resonant inverter with eGaN FET for wireless power transfer, " *IEEE Trans. Power Electron.*, vol. 33, no. 3, pp. 1890-1896, Mar. 2018.

[20] R. E. Zulinski and K. J. Grady, " Load-independent class E power inverter. I. Theoretical development, " *IEEE Trans. Circuits Syst. I*, vol. 37, no. 8, pp. 1010-1018, Aug. 1990.

[21] L. Roslaniec, A. S. Jurkov, A. A. Bastami, and D. J. Perreault, " Design of single-switch inverters for variable resistance / load modulation operation, " *IEEE Trans. Power Electron.*, vol. 30, no. 6, pp. 3200-3214, June 2015.

[22] S. Aldhaher, D. C. Yates, and P. D. Mitcheson, " Load-independent class E/EF inverters and rectifiers for MHz-switching applications, " *IEEE Trans. Power Electron.*, vol. 33, no. 10, pp. 8270-8287, Oct. 2018.

[23] W. Luo, X. Wei, H. Sekiya, and T. Suetsugu, " Design of load-independent class-E inverter with MOSFET parasitic capacitances, " *2019 IEEE 62nd Int. Midwest Symp. Circuits and Syst.*, vol. 33, no. 10, pp. 8270-8287, Dallas, Oct. 2018.

[24] N. Obinata, W. Luo, X. Wei, and H. Sekiya, " Analysis of load-independent class-E inverter at any duty ratio, " *45th Annu. Conf. IEEE Ind. Electron. Soc.*, Lisbon, Oct. 2019.

[25] Y. Komiyama, S. Matsuhashi, W. Zhu, T. Mishima, Y. Ito, T. Uematsu, K. Nguyen, and H. Sekiya, "Frequency-modulation controlled load-independent class-E inverter," *IEEE Access*, vol. 9, pp. 144600-144613, Oct. 2021.

[26] X. Huang, Z. Yu, Y. Dou, S. Lin, Z. Ouyang and M. A. E. Andersen, "Load-independent push-pull class E^2 topology with coupled inductors for MHz-WPT applications," *IEEE Trans. Power Electron.*, vol. 37, no. 7, pp. 8726-8737, July 2022.

[27] M. Mizutani, S. Koyama, S. Abe, and T. Ohira, " Geodesic theory of zero-voltage-switching RF power inverters for constant-voltage or -current output operation, " *IEEE Int. Conf. Power Energy*, Penang, Dec. 2020, pp. 85-90.

[28] A. Ramsay and R.D. Richtmyer, *Introduction to Hyperbolic Geometry*, Springer, New York, 1995.

[29] J. W. Cannon, W. J. Floyd, R. Kenyon, and W. R. Parry, "Hyperbolic geometry," Flavors of Geometry, vol. 31, pp. 59-115, MSRI Publications. http://library.msri.org/books/Book31/contents.html (accessed Oct. 19, 2022)

[30] J. W. Helton, " The distance of a function to H^∞ in the Poincaré metric: electrical power transfer, " Journal of Functional Analysis, vol. 38, no. 2, pp. 273-314, Sept. 1980.

Minoru Mizutani received his M.E. degree from Toyohashi University of Technology (TUT), Aichi, Japan, in 2014. From 2014 to 2019, he developed wireless power transfer technologies for factory automation systems at Murata Machinery, LTD, Japan. From 2019 to 2020, he was a researcher at TUT. Since 2020, he has been a project research associate at TUT. His current research interests include wireless power transfer and power electronics at MHz frequencies. He recieved the IEICE Transactions Paper Award in 2022.

Takashi Ohira received his Ph.D. degree from Osaka University in 1983. He founded two regional chapters for IEEE MTT Society (Kansai Chapter in 2006 and Nagoya Chapter in 2010). He is an URSI Fellow and IEEE Life Fellow. He served as an IEEE Distinguished Microwave Lecturer in 2013-2015. He creates stimulating instructive enigmas monthly on IEEE Microwave Magazine.